metals

Article

Influence of Post-Weld Heat Treatment on the Microstructure, Microhardness, and Toughness of a Weld Metal for Hot Bend

Xiu-Lin Han [1], Da-Yong Wu [2], Xiang-Ling Min [1], Xu Wang [1], Bo Liao [2] and Fu-Ren Xiao [2,*]

1 CNPC Bohai Petroleum Equipment Manufacture Co., Ltd., Qingxian 062658, China; hanxll@sohu.com (X.-L.H.); mxlwjt@163.com (X.-L.M.); sjy_wangxu@163.com (X.W.)

2 Key Laboratory of Metastable Materials Science & Technology, College of Materials Science & Engineering, Yanshan University, Qinhuangdao 066004, China; wudayong@dicastal.com (D.-Y.W.); laorll@aliyun.com (B.L.)

* Correspondence: frxiao@ysu.edu.cn; Tel./Fax: +86-335-807-7110

Academic Editor: Hugo F. Lopez

Received: 31 December 2015; Accepted: 18 March 2016; Published: 25 March 2016

Abstract: In this work, a weld metal in K65 pipeline steel pipe has been processed through self-designed post-weld heat treatments including reheating and tempering associated with hot bending. The microstructures and the corresponding toughness and microhardness of the weld metal subjected to the post-weld heat treatments have been investigated. Results show that with the increase in reheating temperature, austenite grain size increases and the main microstructures transition from fine polygonal ferrite (PF) to granular bainitic ferrite (GB). The density of the high angle boundary decreases at higher reheating temperature, leading to a loss of impact toughness. Lots of martensite/austenite (M/A) constituents are observed after reheating, and to a large extent transform into cementite after further tempering. At high reheating temperatures, the increased hardenability promotes the formation of large quantities of M/A constituents. After tempering, the cementite particles become denser and coarser, which considerably deteriorates the impact toughness. Additionally, microhardness has a good linear relation with the mean equivalent diameter of ferrite grain with a low boundary tolerance angle ($2^\circ - 8^\circ$), which shows that the hardness is controlled by low misorientation grain boundaries for the weld metal.

Keywords: M/A constituent; cementite; toughness; microhardness; EBSD

1. Introduction

Pipeline steels used to transport crude oil or natural gas over long distances under high pressure essentially require extraordinary strength and toughness; thus, numerous studies have been conducted to achieve this purpose. The acicular ferrite (AF) microstructure in pipeline steel, which has been considered to have the optimum mechanical properties, has become the hotspot of study. Xiao *et al.* [1] reported that the ferrite microstructures in pipeline steel were divided into polygonal ferrite (PF), quasi-polygonal ferrite (QF) or massive ferrite (MF), granular bainite (GB), and bainitic ferrite (BF), according to the metallographical identification and classification of the phases. Based on this work, Wang *et al.* [2,3] claimed that AF was a complex consisting of QF, GB, and BF, with dispersed islands of second phases in the matrix. The higher dislocation density and sub-boundaries within QF and GB provided greater strength for the pipeline steel, compared to the conventional PF-pearlite structure. Similar work by Chung *et al.* [4] showed that the strengthening effect can be enhanced by fine ferrite laths, precipitates, and martensite/austenite (M/A) constituents with small island and thin film inside the ferrite structure.

Currently, thermo-mechanical processing is considered as the primary route for developing American Petroleum Institute (API) grade pipeline steels because such a process definitively influences the final microstructure. Most studies have focused on the effect of processing parameters on the microstructure of the pipe body and/or the welding heat-affected zone. However, steel pipe products include not only the straight pipes but also a number of accessories, such as bends. Post-weld heat treatments including reheating and tempering associated with hot bending for the welds in pipeline steels have not received sufficient attention. In particular, limited information is available about the effect of the post-weld heat treatments associated with hot bending on the microstructures and properties of the weld joint. The bends have become a key part of the pipeline project. Therefore, it is necessary to explore the evolution of the microstructure and related properties of the weld metal in pipes during hot bending.

Additionally, to explore the relationship between microstructure and properties, numerous researchers consider the orientation of the ferrite grains with respect to each other via EBSD technology. For example, in the analysis of toughness, Díaz-Fuentes *et al.* [5] reported that the microstructural unit controlling brittle fracture in an acicular ferrite microstructure could be defined as a set of adjacent ferrite plates with crystallographic misorientations below an angle of 15°. For the strength analysis, Iza-Mendia and Gutiérrez [6] revealed that the optical ferrite mean linear intercept was equivalent to the mean equivalent diameter (MED) computed from EBSD scans using a threshold angle of 2°. In this work, the as-received material is a weld metal in K65 pipeline steel. After post-weld heat treatments associated with hot bending, the relationship between microstructure and hardness was analyzed via EBSD.

During the actual hot bending process, the weld metal is usually set up at the top of the pipe, so the plastic deformation can be neglected [7,8]. Therefore, the hot bending process can be simulated by a reheating treatment. Our previous work showed that increasing of Ni content in weld metals could improve the mechanical properties of the weld metals after simulated post-weld heat treatments for hot bends [9], while the effects of post-weld heat treatments on the microstructure and mechanical properties have not sufficiently investigated. In this paper, the effects of post-weld reheating and tempering temperature on the microstructure, toughness, and hardness of the weld metal with high Ni content were investigated.

2. Experimental Materials and Procedure

2.1. Materials and the Post-Weld Heat Treatments

The base metal was a commercial K65 pipeline steel with 1219 mm outside diameter and 30.8 mm wall thickness. The double face four wire tandem submerged arc welding was performed according to the actual welding process for a K65 hot bend. Test pieces of weld metal with the size 10 mm × 10 mm × 80 mm were cut from the outer side of the weld metal transversely to the weld line, as shown in Figure 1. The chemical compositions of the out-side weld metal are shown in Table 1.

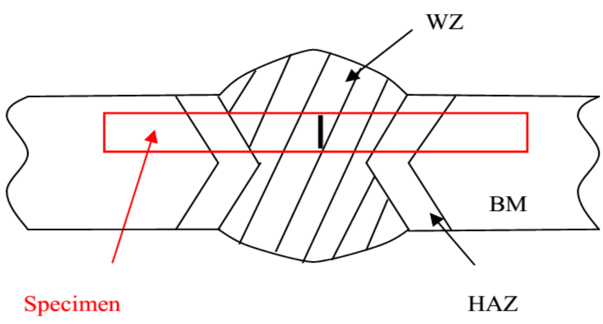

Figure 1. Schematic diagram for sampling method of the impact specimens (WZ: weld zone; HAZ: heat affected zone; BM: base metal).

Table 1. Chemical compositions of the weld metal (wt. %).

Elements	C	Mn	Si	P	S	Mo	Ni	Cr	Cu	V	Nb	Ti	Al	N	B	Ceq [1]	Pcm [2]
Amount	0.06	1.67	0.28	0.019	0.005	0.161	0.52	0.123	0.105	0.01	0.036	0.015	0.019	0.008	0.0008	0.44	0.18

[1] $\mathrm{Ceq} = \mathrm{C} + \frac{\mathrm{Mn}}{6} + \frac{\mathrm{Ni}+\mathrm{Cu}}{15} + \frac{\mathrm{Cr}+\mathrm{Mo}+\mathrm{V}}{5}$; [2] $\mathrm{Pcm} = \mathrm{C} + \frac{\mathrm{Si}}{30} + \frac{\mathrm{Mn}+\mathrm{Cu}+\mathrm{Cr}}{20} + \frac{\mathrm{Ni}}{60} + \frac{\mathrm{Mo}}{15} + \frac{\mathrm{V}}{10} + 5\mathrm{B}$

Post-weld heat treatments were conducted on a Gleeble-3500 thermal simulator (DSI, New York, NY, USA), and the processing schedules are provided in Figure 2. The time from room temperature to reheating temperature was 60 s, and the temperatures ranged from 990 °C to 1080 °C. After maintaining the reheating temperature for 60 s, some quenched samples were obtained for prior austenite grain size observation and others were cooled to room temperature at a cooling rate of 10 °C/s. Finally the samples were tempered at 550 °C and 680 °C, respectively, to simulate the post-weld treatments associated with an industrial hot bending production process as closely as possible.

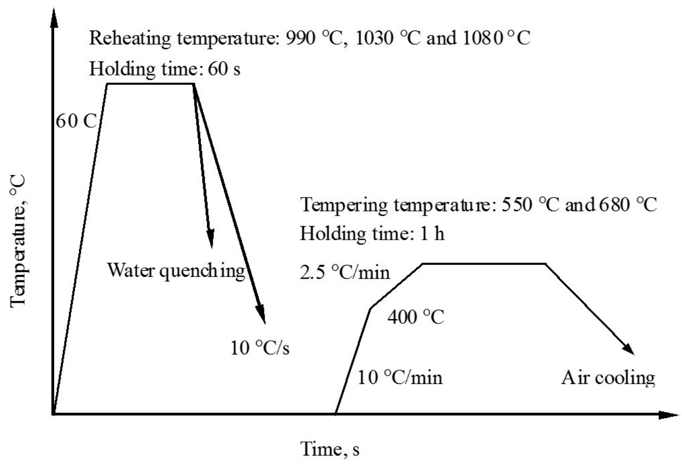

Figure 2. Schematic illustration of post-weld heat treatment schedule for experimental weld metal.

2.2. Mechanical Properties

The low-temperature impact toughness and microhardness of the specimens subjected to the reheating and tempering processes were measured. Charpy impact tests were performed at −40 °C using the Charpy V-notch (CVN) specimens in accordance with the standard of ASTME23-02. The V-notch was machined at the center of the weld metal in the cross section of the weld. The toughness values were calculated as an average of three measurements. The Vickers microhardness was measured using a FM-ARS 9000 hardness testing machine (Future-Tech, Tokyo, Japan) at a load of 500 gf, and the indentation area was selected randomly in the weld metal. The hardness test results represented the average of five measurements.

2.3. Microstructural Characterization

The CVN specimen fracture surface was observed by using a KYKY-2800 scanning electron microscope (SEM) (KYKY, Beijing, China) to examine the cleavage fracture and the crack propagation path. Specimens derived from the transverse cross section planes of the steels were mechanically polished and etched by a 3% nital solution. The microstructures were then observed by using a Hitachi S-4800 SEM (Hitachi, Tokyo, Japan). The initial austenite grain boundaries were observed on quenched specimens etched in an aqueous picric acid solution. To observe the M/A constituent, the LePera reagent of 1 g sodium metabisulfite in 100 mL of distilled water, mixed with 4 g of picric acid dissolved in 100 mL of alcohol was used. The M/A constituents were identified by optical microscopy (OM, Zeiss, Oberkochen, Germany). Samples for the electron backscatter diffraction (EBSD) analyzer

(EDAX, Mahwah, NJ, USA) were electrolytically polished in a solution of 8% perchloric acid and 92% ethanol. The EBSD maps were analyzed by Channel 5 software (TSL OIM 7, EDAX, Mahwah, NJ, USA, 2011) from Oxford-HKL. Thin foils for transmission electron microscopy (TEM) were prepared by mechanical thinning from 300 μm to 50 μm, along with twin-jet electropolishing in an electrolyte of 8% perchloric acid and 92% ethanol; and the examinations were performed using a JEM-2010 TEM (JEOL, Tokyo, Japan) with 200 kV.

3. Results

3.1. Properties

Charpy impact energy (−40 °C) and Vicker's hardness results of the samples under different conditions are listed in Table 2. The tempered specimens reheated at 990 °C and 1030 °C achieved satisfactory impact toughness energy within 86 J to 133 J. The values of impact energy, 24 J to 29 J, were significantly lower for the tempered specimens reheating at 1080 °C. The microhardness of the tempered specimens reheated at 990 °C and 1030 °C was higher than that of the tempered specimens reheated at 1080 °C.

Table 2. Toughness and microhardness of the weld metal.

Reheating Temperature (°C)	Tempering Temperature (°C)	Charpy Impact Energy (−40 °C, J)			Microhardness (HV)		
		Discrete Values	Average Value	Error Range	Discrete Values	Average Value	Error Range
990	550	115, 152, 126	131	±21	248, 257, 257, 246, 253	252	±6
	680	109, 132, 146	129	±20	249, 254, 252, 230, 250	247	±17
1030	550	138, 143, 118	133	±15	268, 250, 256, 259, 249	256	±12
	680	96, 92, 70	86	±16	255, 259, 259, 254, 243	254	±11
1080	550	45, 18, 24	29	±16	230, 238, 244, 229, 232	235	±9
	680	16, 19, 37	24	±13	229, 238, 235, 235, 220	231	±11

3.2. Microstructure

The prior austenite grain and microstructures after reheating at different temperatures are shown in Figure 3. The grain size of austenite varied insignificantly at 990 °C and 1030 °C, while it increased markedly at 1080 °C (Figure 3a–c). This was associated with the quick dissolution of fine Nb precipitates at a higher reheating temperature [10]. The prior austenite microstructures were also affected on the cooled microstructures. When the reheating temperature was 990 °C, the precipitates hardly dissolved, the austenite grain size was relatively small, and the alloy elements distribution was heterogeneous, so the phase transformation temperature was higher. The main microstructures were PF and QF (Figure 3d). A high austenitizing temperature could improve austenite's homogeneity and hardenability; otherwise it is prone to form low-temperature microstructures. Therefore, a mixed microstructure of fine QF and GB was obtained at 1030 °C (Figure 3e), and the microstructure changed to mainly coarse GB at 1080 °C (Figure 3f). Additionally, as the ferrite nucleated and grew, partitioning of carbon took place at the austenite-ferrite interface; the austenite-enriched carbon would transform to its M/A constituent.

After tempering, the PF and QF showed little change, while the GB and M/A constituent changed remarkably because the recovery and recrystallization occurred in parts of GB, resulting in smaller PF grains distributed at the lath ferrite boundary [11,12], as clearly illustrated in Figure 4. Wang *et al.* [3]

claimed that PF generally grows into equiaxed grains with smooth and continuous boundaries. However, QF boundaries are irregular and jagged, even discontinuous. BF consists of many elongated parallel ferritic laths. Compared to BF, GB contains irregular ferritic laths with no clear boundaries. According to different microstructural characteristics, different ferrites of PF, QF, and GB have been marked. In addition, degenerate pearlite was observed after tempering at 550 °C, as is shown in Figure 5a. There were two kinds of particles observed in the SEM micrographs: one was proven to be Ti-oxide in the weld metal (Figure 5b), randomly distributed in the microstructure, which could serve as the nucleation site of intra-granular ferrite; another kind, mainly distributed on the grain boundaries, was identified as carbides, produced by the tempering transformation of the M/A constituents (Figure 5c). With increasing tempering temperatures, the degenerate pearlite disappeared while the amount of carbides allocated on the grain boundaries increased.

The evolution of the M/A constituent through reheating at different temperatures, before and after tempering at 550 °C, is presented in Figure 6. Before tempering, a large amount of M/A islands were dispersed in the ferrite matrix when reheating at 990 °C and 1030 °C. However, for the specimen reheating at 1080 °C, the M/A constituent not only distributed in the ferritic matrix, but also segregated on the prior austenite grain boundaries. After tempering, the amount of M/A islands decreased sharply and the retained M/A islands were refined.

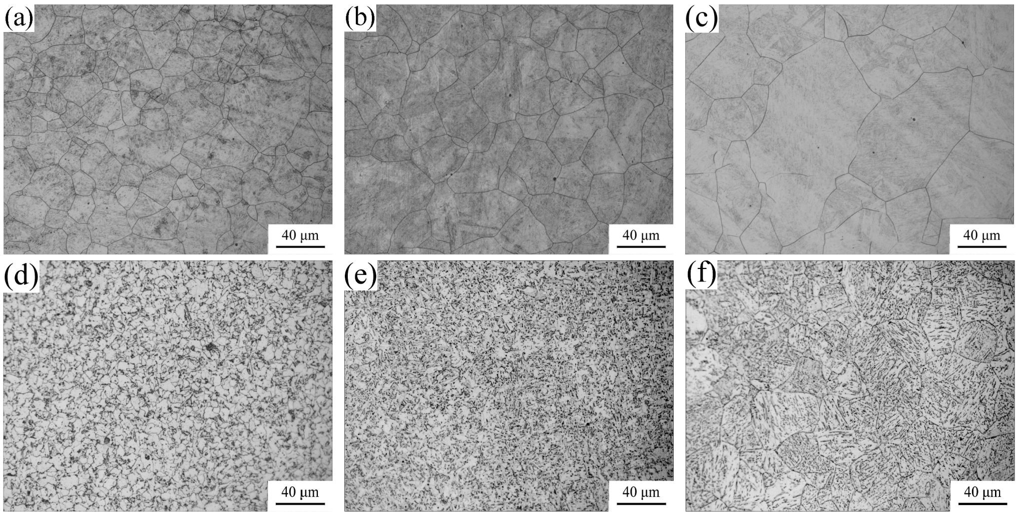

Figure 3. Optical images of prior austenite grain boundary (**a**–**c**) and microstructures (**d**–**f**) at different reheating temperatures: (**a**,**d**) 990 °C; (**b**,**e**) 1030 °C; (**c**,**f**) 1080 °C.

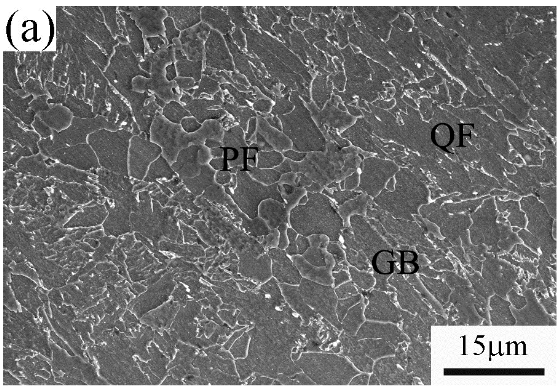

Figure 4. *Cont.*

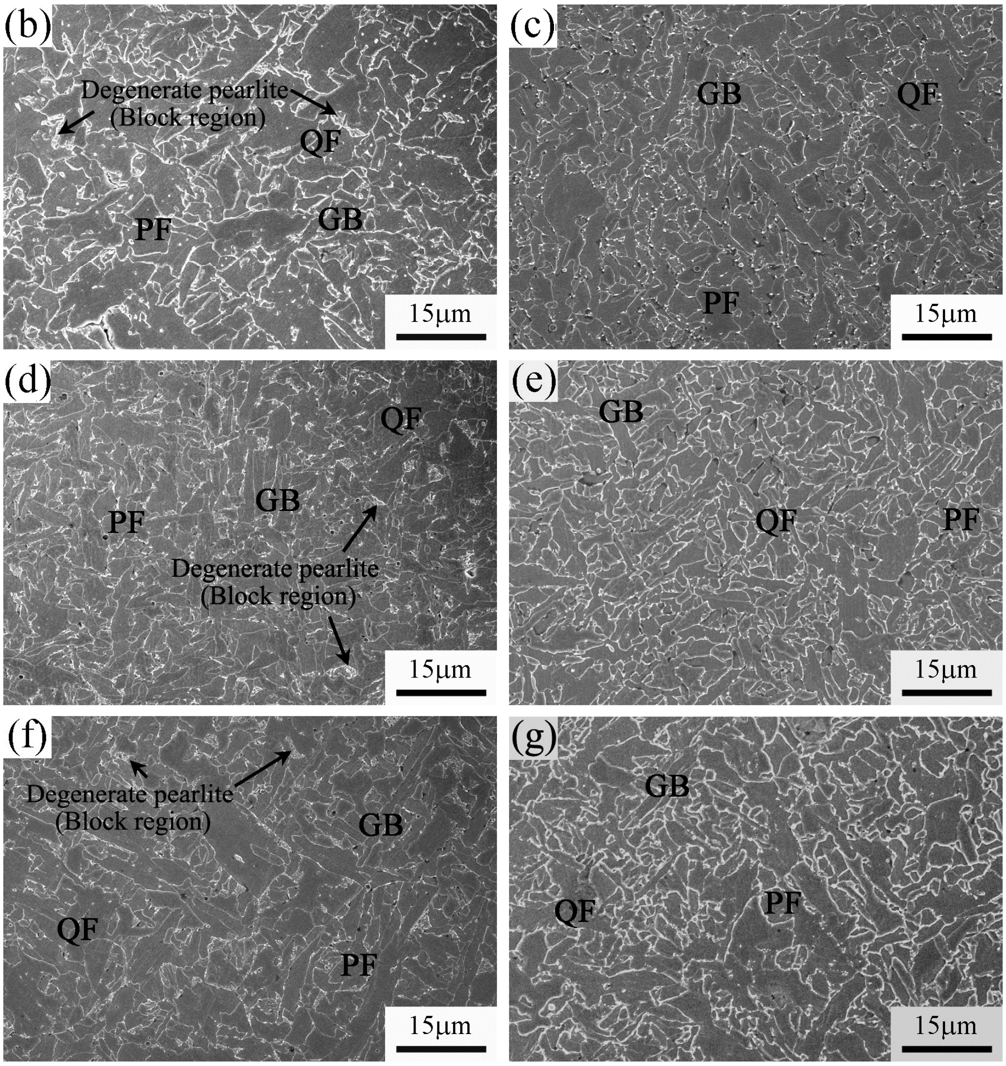

Figure 4. SEM micrograph for specimens treated under different conditions: (**a**) Prior to treatments; (**b**) RT = 990 °C, TT = 550 °C; (**c**) RT = 990 °C, TT = 680 °C; (**d**) RT = 1030 °C, TT = 550 °C; (**e**) RT = 1030 °C, TT = 680 °C; (**f**) RT = 1080 °C; TT = 550 °C; (**g**) RT = 1080 °C, TT = 680 °C. (RT: reheating temperature; TT: tempering temperature).

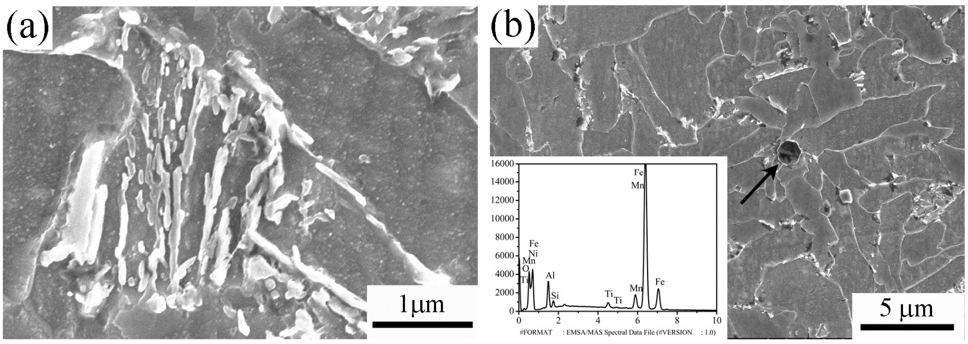

Figure 5. *Cont*.

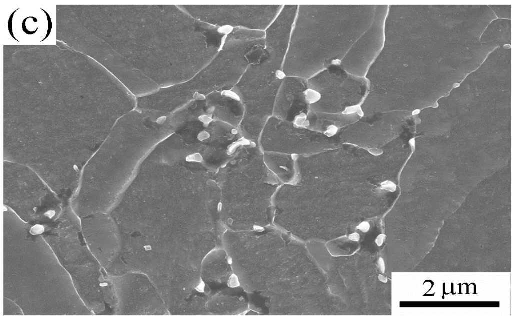

Figure 5. SEM micrographs for degenerate pearlite (**a**); intra-granular ferrite nucleated around Ti-oxide particle (insert: EDX result of Ti-oxide particle) (**b**), and carbides (**c**) in specimens reheated at 990 °C; tempering at 550 °C (**a**,**b**) and 680 °C (**c**).

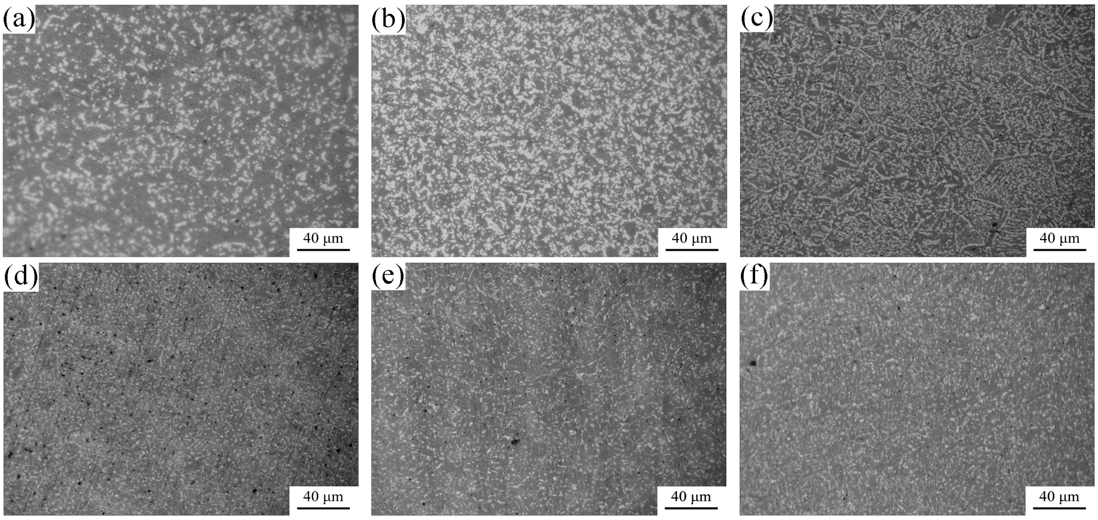

Figure 6. M/A constituent observations of the samples reheated at different temperatures (990 °C (**a**); 1030 (**b**); 1080 (**c**)) before tempering and after tempering at 550 °C (reheated at 990 °C (**d**); 1030 °C (**e**); 1080 °C (**f**)).

3.3. Particles

Multiple-scale particles were observed via TEM. One of them with approximately 0.5 μm to 1.5 μm was identified as Ti-oxide (Figure 7a). A mass of intra-granular ferrite nucleated on Ti-oxides was observed. Early work by Shim *et al.* [13] examined the potency of various inclusions and precipitates, e.g., MnS, Ti_2O_3, VN, $TiMn_2O_3$, NbC, VC, AlN for the nucleation of intra-granular ferrite, and found that $TiMn_2O_3$ particles showed great efficacy in inducing intra-granular ferrite. The addition of Ti_2O_3 nanoparticles to the weld metal was required in order to increase the density of the ferrite nucleation site. Therefore, a high density of fine ferrite was achieved, which was beneficial to the improvement of strength and toughness. The second particle, with a size of approximately 200 nm to 500 nm, was a carbide identified as cementite (Figure 7b). The coarse cementite particles embellishing the prior austenite grain boundaries resulted in the deterioration of toughness, because stress concentration occurred at the boundaries during the impact process, and the coarse cementite particles easily became crack initiations under an applied stress, which eventually reduced the impact toughness. The third particle type with a size of approximately 50 nm to 200 nm was alloyed precipitates, including NbC, VC, AlN, and composite precipitates (Figure 7c).

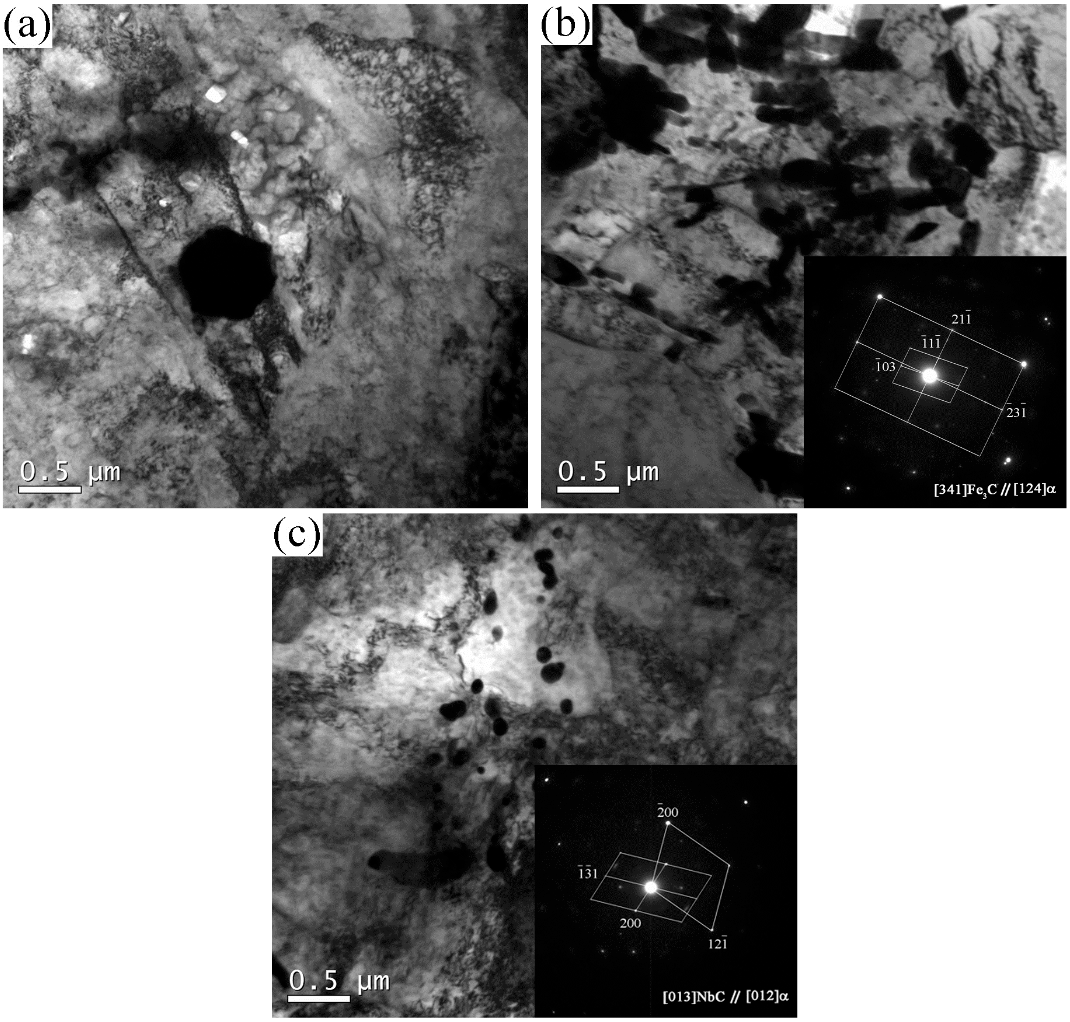

Figure 7. TEM images for the three scales particles in specimens: (**a**) Ti-oxide; (**b**) cementite decomposed from M/A island (insert: diffraction pattern); (**c**) MC carbides precipitated in matrix (insert: diffraction pattern).

3.4. EBSD Analysis of the Microstructures

Figure 8 shows the inverse pole figures (IPF) of the ferrite phase with boundary misorientation maps obtained from EBSD measurement of the specimens after the whole heat treatments. Capdevila *et al.* [14] reported that the boundaries with misorientations of 15° or higher can force a crack to change its propagation path during cleavage fracture to efficiently inhibit cleavage crack propagation. Therefore, the density of high angle grain boundary is an important consideration to control and characterize toughness. It is proposed that the mean equivalent diameter of the ferrite effective grain with a tolerance angle of 15° ($(MED)_{15^\circ}$) and the fraction of high angle boundary dominate the density of high angle boundary. The related data are summarized in Table 3. As shown in Table 3, only the $(MED)_{15^\circ}$ obtained under reheating at 1080 °C was larger than that obtained under reheating at 990 °C or 1030 °C. The fractions of high angle boundary in the specimens reheated at 990 °C and 1030 °C were similar, whereas that of specimens reheated at 1080 °C was significantly lesser. As the tempering temperature increased from 550 °C to 680 °C, the fraction of high angle boundary changed slightly, but the low angle boundary fraction increased. Therefore, the impact energy decreased with the increase of reheating and tempering temperatures (Table 2).

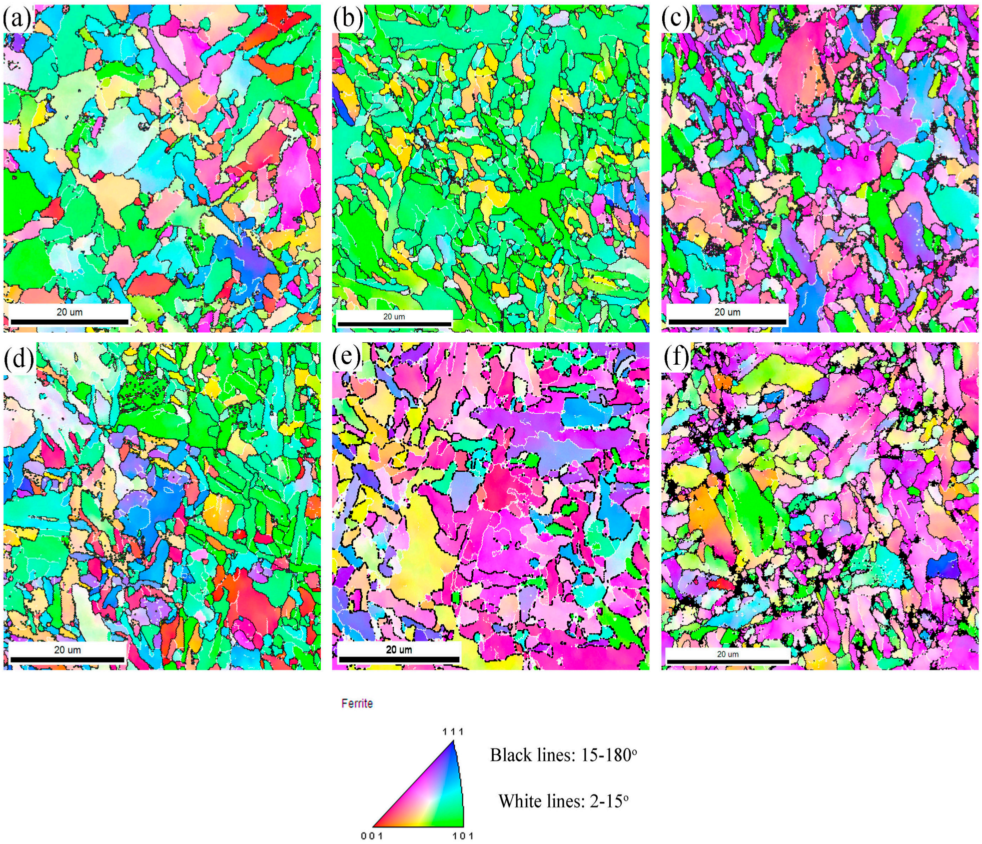

Figure 8. Inverse pole figure maps obtained from EBSD measurement of the specimens treated under different conditions: (**a**) RT = 990 °C, TT = 550 °C; (**b**) RT = 990 °C, TT = 680 °C; (**c**) RT = 1030 °C, TT = 550 °C; (**d**) RT = 1030 °C, TT = 680 °C; (**e**) RT = 1080 °C; TT = 550 °C; (**f**) RT = 1080 °C, TT = 680 °C (RT: reheating temperature; TT: tempering temperature).

Table 3. EBSD results of the microstructural quantification.

Reheating Temperature (°C)	Tempering Temperature (°C)	Fraction of Low Angle Boundaries, %	Fraction of High Angle Boundaries, %	$(MED)_{2°}$ (μm)	$(MED)_{15°}$ (μm)
990	550	15.8	57.3	2.7	3.5
	680	21.4	58.7	2.8	3.3
1030	550	11.2	58.8	2.3	3.2
	680	16.3	54.6	2.5	3.1
1080	550	17.2	36.3	3.9	4.8
	680	18.2	17.6	4.1	4.7

According to the study by Iza-Mendia and Gutiérrez [6], the smallest microstructural unit size contributing to grain boundary strengthening was the effective grain with a tolerance angle of 2°. A small mean equivalent diameter of grain with a tolerance angle of 2° ($(MED)_{2°}$) will result in a better strengthening effect. The $(MED)_{2°}$ under reheating at 1080 °C was larger than that under reheating at 990 or 1030 °C.

In addition, in this work, we did not find large amounts of small alloyed precipitates with dispersed distribution in all specimens. Moreover, the dislocation hardening was minor compared to other terms and during long-term tempering, the dislocation density decreased because of the occurrence of recovery. Hence, the contribution of alloyed precipitation and dislocation density to microhardness appeared to be similar for the specimens after different post-weld heat treatments. Therefore, grain size is a very important factor that affects the hardness. Figure 9 shows the relationship of the values of microhardness with a function of MED at a tolerance angle of 2° to 15°. The current results were in good agreement with this method, but when θ ⩾ 8°, the fitting results were less satisfying, which revealed that hardness was controlled by low misorientation grain boundaries.

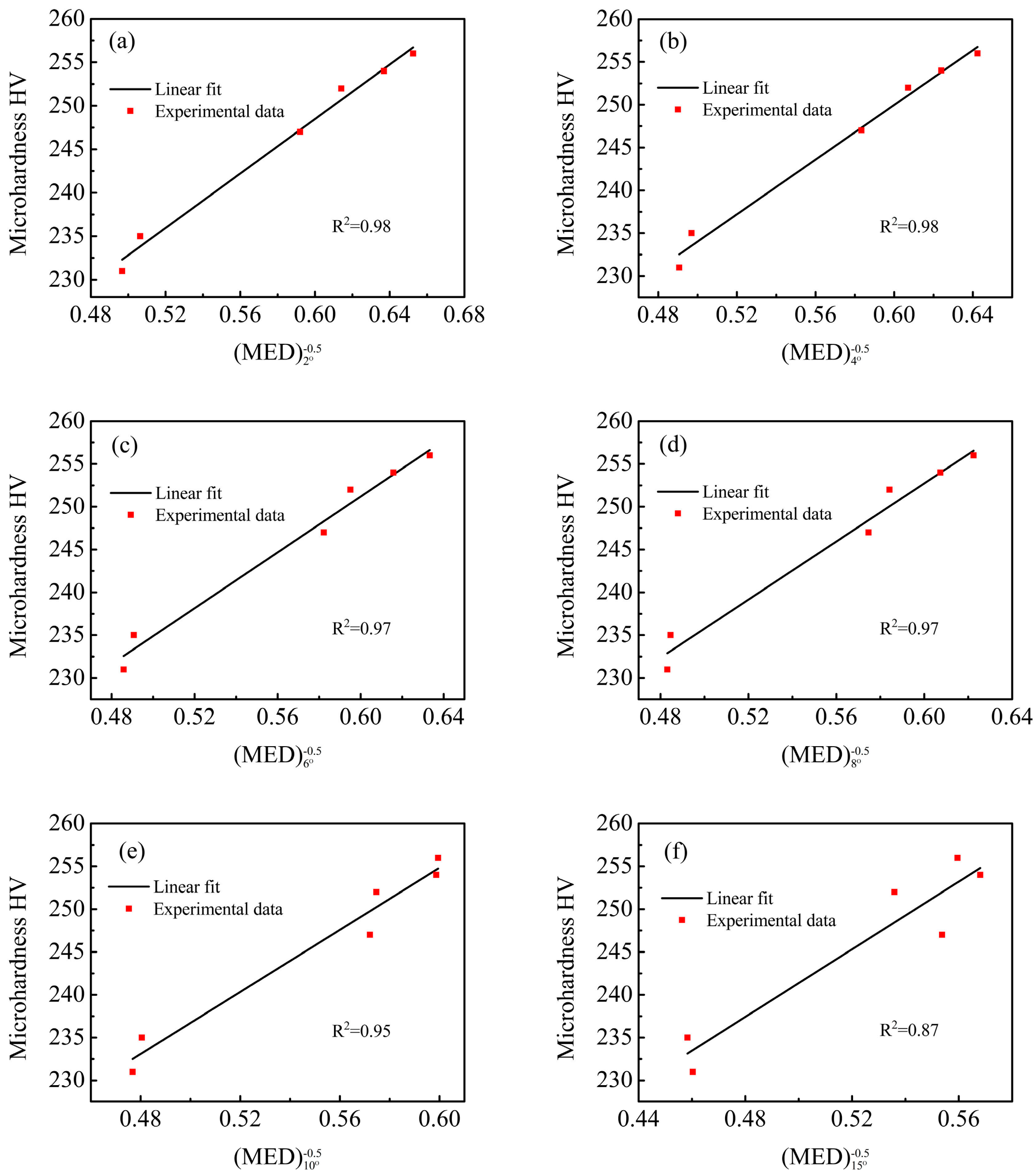

Figure 9. Microhardness of the test steel varied with the reciprocal square root of effective grain size with different tolerance angles: (**a**) 2°; (**b**) 4°; (**c**) 6°; (**d**) 8°; (**e**) 10°; (**f**) 15°.

4. Conclusions

(1) At a higher reheating temperature, austenite grows rapidly and leads to a low-temperature microstructure. The low density of high angle grain boundary in the microstructure after tempering deteriorates the impact toughness.

(2) At higher reheating temperature, a large amount of M/A constituents are obtained; they develop into clusters and coarsen after tempering. An increased possibility of microcrack formation is accompanied by a loss of impact toughness.

(3) Within the range of tempering temperature in the work, increasing the tempering temperature makes little difference to the low density of high angle grain boundary, but accelerates the decomposition of the M/A constituents.

(4) EGS contributed most to hardness and had a good linear relationship with the microhardness in the range of tolerance angle 2°–8°.

Acknowledgments: This work was financially supported by the Natural Science Foundation of China (51171162) and the Hebei Provincial Key Technology Support Program (14211010D, 15211019D).

Author Contributions: The experiments were arranged by Xiu-Lin Han, Da-Yong Wu and Xiang-Ling Min. The experiments were conducted by Xu Wang, Xiu-Lin Han and Fu-Ren Xiao. The article was written by Xiu-Lin Han and revised by Bo Liao and Fu-Ren Xiao.

Conflicts of Interest: The authors declare no conflict of interest.

References

1. Xiao, F.R.; Liao, B.; Ren, D.L.; Shan, Y.Y.; Yang, K. Acicular ferritic microstructure of a low-carbon Mn-Mo-Nb microalloyed pipeline steel. *Mater. Charact.* **2005**, *54*, 305–314. [CrossRef]
2. Wang, W.; Yan, W.; Zhu, L.; Hu, P.; Shan, Y.Y.; Yang, K. Relation among rolling parameters, microstructures and mechanical properties in an acicular ferrite pipeline steel. *Mater. Des.* **2009**, *30*, 3436–3443. [CrossRef]
3. Wang, W.; Shan, Y.Y.; Yang, K. Study of high strength pipeline steels with different microstructures. *Mater. Sci. Eng. A* **2009**, *502*, 38–44. [CrossRef]
4. Chung, P.C.; Ham, Y.; Kim, S.; Lim, J.; Lee, C. Effects of post-weld heat treatment cycles on microstructure and mechanical properties of electric resistance welded pipe welds. *Mater. Des.* **2012**, *34*, 685–690. [CrossRef]
5. Díaz-Fuentes, M.; Iza-Mendia, A.; Gutiérrez, I. Analysis of different acicular ferrite microstructures in low-carbon steels by electron backscattered diffraction. Study of their toughness behavior. *Metall. Mater. Trans. A* **2003**, *34*, 2505–2516. [CrossRef]
6. Iza-Mendia, A.; Gutiérrez, I. Generalization of the existing relations between microstructure and yield stress from ferrite-pearlite to high strength steels. *Mater. Sci. Eng. A* **2013**, *561*, 40–51. [CrossRef]
7. Tang, N.C. Plastic-deformation analysis in tube bending. *Int. J. Pres. Vessel. Pip.* **2000**, *77*, 751–759. [CrossRef]
8. Hu, Z.; Li, J.Q. Computer simulation on pipe bending processes with small bending radius by using local induction heating. *J. Mater. Process. Technol.* **1999**, *91*, 75–79. [CrossRef]
9. Wu, D.Y.; Han, X.L; Tian, H.T.; Liao, B.; Xiao, F.R. Microstructural characterization and mechanical properties analysis of weld metals with two Ni contents during post-weld heat treatments. *Metall. Mater. Trans. A* **2015**, *46*, 1973–1984. [CrossRef]
10. Banerjee, K.; Militzer, M.; Perez, M.; Wang, X. Nonisothermal austenite grain growth kinetics in a microalloyed X80 linepipe steel. *Metall. Mater. Trans. A* **2010**, *41*, 3161–3172. [CrossRef]
11. Zhu, Z.; Kuzmikova, L.; Li, H.; Barbaro, F. Effect of inter-critically reheating temperature on microstructure and properties of simulated inter-critically reheated coarse grained heat affected zone in X70 steel. *Mater. Sci. Eng. A* **2014**, *605*, 8–13. [CrossRef]
12. Hu, J.; Du, L.X.; Wang, J.J.; Xie, H.; Gao, C.R.; Misra, R.D.K. High toughness in the intercritically reheated coarse-grained (ICRCG) heat-affected zone (HAZ) of low carbon microalloyed steel. *Mater. Sci. Eng. A* **2014**, *590*, 323–328. [CrossRef]
13. Shim, J.H.; Oh, Y.J.; Suh, J.Y.; Cho, Y.W.; Shim, J.D.; Byun, J.S.; Lee, D.N. Ferrite nucleation potency of non-metallic inclusions in medium carbon steels. *Acta Mater.* **2001**, *49*, 2115–2122. [CrossRef]
14. Capdevila, C.; Garcia-Mateo, C.; Chao, J.; Caballero, F.G. Effect of V and N Precipitation on Acicular Ferrite Formation in Sulfur-Lean Vanadium Steels. *Metall. Mater. Trans. A* **2009**, *40*, 522–538. [CrossRef]